ADVANCED FUNCTIONAL MATERIALS
www.afm-journal.de

Advanced Electroactive and Anti-Inflammatory Sutures for Enhancing Tendon and Bone Regeneration to Promote Repair of Achilles Tendon Sleeve Avulsion

Xiao Yu, Chao Li, Jie Cui, Hao Feng, Yangfan Ding, Jiahui Song, Pengfei Cai, Liang Chen, Mohamed EL-Newehy, Meera Moydeen Abdulhameed, Xiumei Mo, Yu Han,* and Binbin Sun**

Achilles tendon sleeve avulsions often involve tissue defects. Standard bone tunnel fixation risks tunnel enlargement, inflammation, and graft failure. Native tendon and bone tissue exhibit inherent bioelectrical properties whose disruption impedes healing. To address these, the study developed electroactive, anti-inflammatory sutures featuring a strong polylactic acid (PLA) micron yarn core and a conductive poly(3,4-ethylenedioxythiophene)/hydroxyethyl cellulose/glycerol/chondroitin sulfate/PLA (PEDOT/HEC/glycerol/CS/PLA) nanofibrous shell. A novel synthesis strategy enabled EDOT polymerization templated by HEC, eliminating the need for poly(styrene sulfonate) (PSS), oxidants, or catalysts and allowing direct electrospinning. In vitro, it can regulate macrophage polarization and enhance tenocytes and bone marrow mesenchymal stem cell (BMSCs) proliferation and differentiation. In a rabbit Achilles tendon avulsion model, the suture enables secure tendon-to-bone fixation via calcaneal bone tunnels. At 12 weeks post-operation, the suture exerts anti-inflammatory effects by modulating CD206/CD86 expression. Electroactive suture significantly enhances tendon regeneration and bone formation within the tunnels, and achieves robust tendon-to-bone integration at the interface, markedly improving fixation stability. In summary, this electroactive, anti-inflammatory suture effectively promotes tendon-bone regeneration for repairing Achilles tendon sleeve avulsions.

1. Introduction

Tendons transmit muscular forces to bones, enabling body movement through their unique biomechanical properties.[1] The Achilles tendon, with its broad insertion at the calcaneal tuberosity, experiences concentrated shear stresses that predispose it to avulsion fractures.[2] When complete detachment occurs as a continuous "sleeve" from the calcaneal insertion without substantial bone fragments – termed Achilles tendon sleeve avulsion – minimal residual tendon tissue remains for surgical repair.[3,4] Crucially, the collagen-rich microstructure of bone and tendon confers inherent piezoelectricity, generating endogenous bioelectric fields under mechanical deformation.[5,6] Injury disrupts this electromechanical microenvironment, impairing healing cascades. Although rare, this pathology severely compromises the triceps surae-calcaneal complex, posing complex reconstructive challenges.[7]

X. Yu, J. Cui, H. Feng, Y. Ding, J. Song, X. Mo, B. Sun
State Key Laboratory for Modification of Chemical Fibers and Polymer Materials, Shanghai Engineering Research Center of Nano-Biomaterials and Regenerative Medicine, College of Biological Science and Medical Engineering
Donghua University
Shanghai 201620, China
E-mail: xmm@dhu.edu.cn; binbin.sun@dhu.edu.cn

C. Li, Y. Han
Department of Orthopaedics, Medical 3D Printing Center
The First Affiliated Hospital of Zhengzhou University
Zhengzhou 450052, China
E-mail: fcchany@zzu.edu.cn

P. Cai
G.E.R.N. Research Center for Tissue Replacement, Regeneration & Neogenesis, Department of Orthopedics and Trauma Surgery, Faculty of Medicine
Medical Center-Albert-Ludwigs-University of Freiburg
79085 Freiburg im Breisgau, Germany

L. Chen
Zhongshan Hospital of Traditional Chinese Medicine Affiliated to Guangzhou University of Traditional Chinese Medicine
Guangzhou 528400, China

M. EL-Newehy, M. M. Abdulhameed
Department of Chemistry, College of Science
King Saud University
P.O. Box 2455, Riyadh 11451, Saudi Arabia

The ORCID identification number(s) for the author(s) of this article can be found under https://doi.org/10.1002/adfm.202516062

DOI: 10.1002/adfm.202516062

Surgical repair requires reattaching the tendon to the bone, typically achieved through anchors or sutures.[8] However, inherent instability at the junction with the bone often causes repair failure:[9,10] i) Tradational biologically inert materials impede osseointegration, ii) non-degradable anchors induce osteolysis through chronic inflammation, iii) the traditional sutures provoke bone tunnel widening via windshield wiper effect and bungee effect, iv) traditional grafts or materials cannot restore the electromyogenic microenvironment of tendons and bones. Current interventions—including end-to-end repair and grafts—fail to fully restore Achilles function, with re-rupture rates of 1.7–5.6%.[11] In addition, dysregulated inflammatory responses further compromise outcomes.[12] Therefore, multifunctional sutures delivering integrated electroactivity, anti-inflammatory modulation, and stable mechanical traction are essential to achieve functional tendon-to-bone regeneration with reconstruction stability.

Advanced electroactive biomaterials enhance microenvironmental conductivity, enabling localized electrical stimulation (ES) delivery for tissue regeneration.[13] Poly (3,4-ethylenedioxythiophene) (PEDOT) fulfills this requirement through its conjugated backbone, where π-electron delocalization establishes charge transport pathways.[14] Chemical/electrochemical doping oxidizes PEDOT chains, generating charge carriers that boost conductivity.[15] Conventional PEDOT: poly(styrene sulfonate) (PEDOT: PSS) dispersions achieve high conductivity yet are predominantly processable in aqueous media,[16,17] necessitating dip-coating deposition that limits applications.[18,19] The strong acidity and inherent cytotoxicity of PSS not only limit its short-term biocompatibility but also impede its long-term integration with host tissues, functional reconstruction, and safe clearance.[20,21] Furthermore, the presence of residual oxidants/catalysts from PEDOT: PSS synthesis poses a significant risk for biological applications.[22] To overcome these, this study exploits hydroxyethyl cellulose (HEC), which has exceptional dispersing capability.[23] Thus, HEC can be used to assist the dispersion of PEDOT in non-aqueous solvents. HEC's hydroxyl groups not only facilitate modification through interactions with other materials but also adsorb ions to create supplementary conductive channels.[24,25] Glycerol is a polyhydroxy compound with good biocompatibility and can be used as a dopant to improve PEDOT conductivity.[26] Both HEC and glycerol can improve the flexibility of the material,[27] so the composite of PEDOT/HEC/glycerol may have greater application potential in electroactive tissue scaffolds.

While traditional sutures satisfy mechanical demands, they remain incapable of integrating electroactivity, anti-inflammatory regulation, and pro-regenerative properties. Electrospinning overcomes this limitation by fabricating core-shell structured sutures. The core-layer yarn provides robust mechanical support for the suture, such as polylactic acid (PLA) micron yarn.[28,29] The shell-layer nanofibers endow sutures with multifunctionality, including superior biocompatibility, large specific surface area, and the ability to facilitate tenocytes and BMSCs adhesion while guiding tissue regeneration.[30] Notably, chondroitin sulfate (CS), a common component of tendon and bone, is incorporated into nanofibers to accelerate tissue formation. The glycosaminoglycan component of the tendon contains CS, which is related to collagen and improves biomechanical properties.[31] Concurrently, CS promotes osteoblast migration and osteogenic differentiation.[32] In addition, CS has anti-inflammatory effects and can balance excessive inflammatory reactions, providing a strong foundation for early tissue repair.[33]

To address the critical unmet needs for sutures that integrate electroactivity, anti-inflammatory modulation, and robust mechanical support for functional tendon-to-bone regeneration, this study developed an electrospun nanofiber-based conductive core-shell suture specifically for reattaching ruptured Achilles tendons in sleeve avulsion injuries to the calcaneus. The shell nanofibers contained HEC, PEDOT, glycerin, PLA, and CS. Within the hexafluoroisopropanol solvent system, hydrogen bond interactions between HEC and EDOT. Therefore, HEC could serve as a template to guide EDOT to polymerize in a certain direction and sequence, which was beneficial for forming a regular PEDOT structure. Glycerin enhanced PEDOT conductivity, while PLA improved the spinnability of the solution and conferred mechanical robustness to the shell fibers. CS provided a further boost to the regeneration of tendon and bone tissue, as well as effectively balancing inflammation. The bundled PLA micron yarn in the core layer provided the essential mechanical of the suture and strong support for postoperative activities. We hypothesized that this multifunctional design would promote healing. Therefore, in vitro experiments were conducted to assess the suture's anti-inflammatory, osteogenic, and tenogenic properties. In vivo studies evaluated its efficacy in surgically re-approximating and securing the ruptured tendon sleeve to the calcaneal bone. Finally, long-term postoperative repair assessments were performed to evaluate the combined contribution of the suture's electroactivity and anti-inflammatory modulation to functional recovery within the challenging Achilles tendon sleeve avulsion model.

2. Results

2.1. Spinning Solution and Suture Fabrication

The sutures were successfully fabricated according to **Figure 1** for tendon-to-bone reattachment. Four formulations were prepared based on their composition:

(i) PGH: PLA (0.25 g), glycerol (0.5 g), HEC (0.5 g)
(ii) PGHE: PGH components + EDOT (0.5 g)
(iii) PGHE-CS2: PGHE components + CS (200 mg)
(iv) PGHE-CS4: PGHE components + CS (400 mg)

Each formulation was dissolved in 16 mL of hexafluoroisopropanol (HFIP) under constant agitation at 46 °C until homogeneous solutions formed. During processing, PGHE, PGHE-CS2, and PGHE-CS4 solutions darkened progressively from white to black, indicating EDOT polymerization to PEDOT. Upon color stabilization, 500 µL ethyl alcohol was added to each solution, followed by 1 min vigorous stirring before electrospinning.

The spinning solution was equally distributed into two syringes and positioned at the positive and negative electrodes of the electrospinning apparatus. Under the applied voltage (±12 kV) and controlled by the winding roller (400 rpm), nanofibers were ejected from the syringe and deposited onto the suspended PLA micron yarn core within the winding roller, forming the core-shell yarn structure. To enhance mechanical properties, multiple core-shell yarns were combined, suspended within

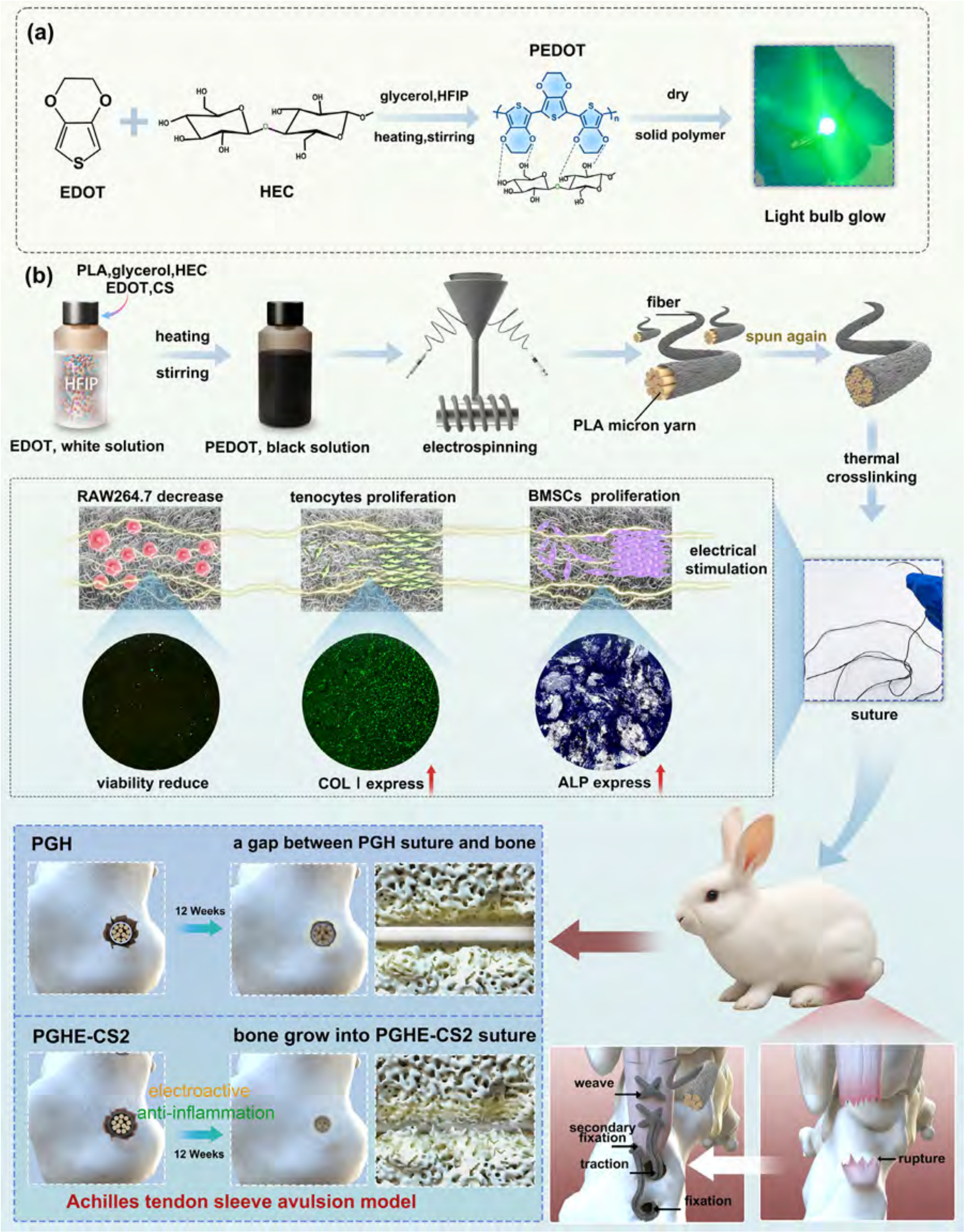

Figure 1. Synthesis mechanism and fabrication process of electroactive and anti-inflammatory sutures for tendon-to-bone reattachment. a) HEC and EDOT were interconnected through hydrogen bonds, and HEC provided a template for the polymerization of EDOT, forming stable PEDOT and achieving dry polymer conductivity. The schematic workflow b): First, solution preparation: the PLA, glycerol, HEC, EDOT, and CS were dissolved in HFIP, forming an initial white solution. Thermal stirring induced EDOT polymerization, progressively changing the solution color to a stable black. Second, suture fabrication: Primary electrospinning deposited nanofibers onto the PLA micron yarn, forming core-shell yarns. Bundled core-shell yarns underwent secondary electrospinning for reinforcement, followed by thermal crosslinking to finalize the suture. Then, in vitro functionality: Under ES, the suture could promote the proliferation and differentiation of tenocytes and BMSCs. CS reduced the macrophages' viability and produced anti-inflammatory effects. Finally, in vivo performance: PGHE-CS2 suture could weave tendon, pass through the bone tunnel, and fix the bone in a rabbit Achilles tendon sleeve avulsion model. After 12 weeks, the new bone gradually grew into the bone tunnel, so the ruptured tendon was stably fixed on the bone.

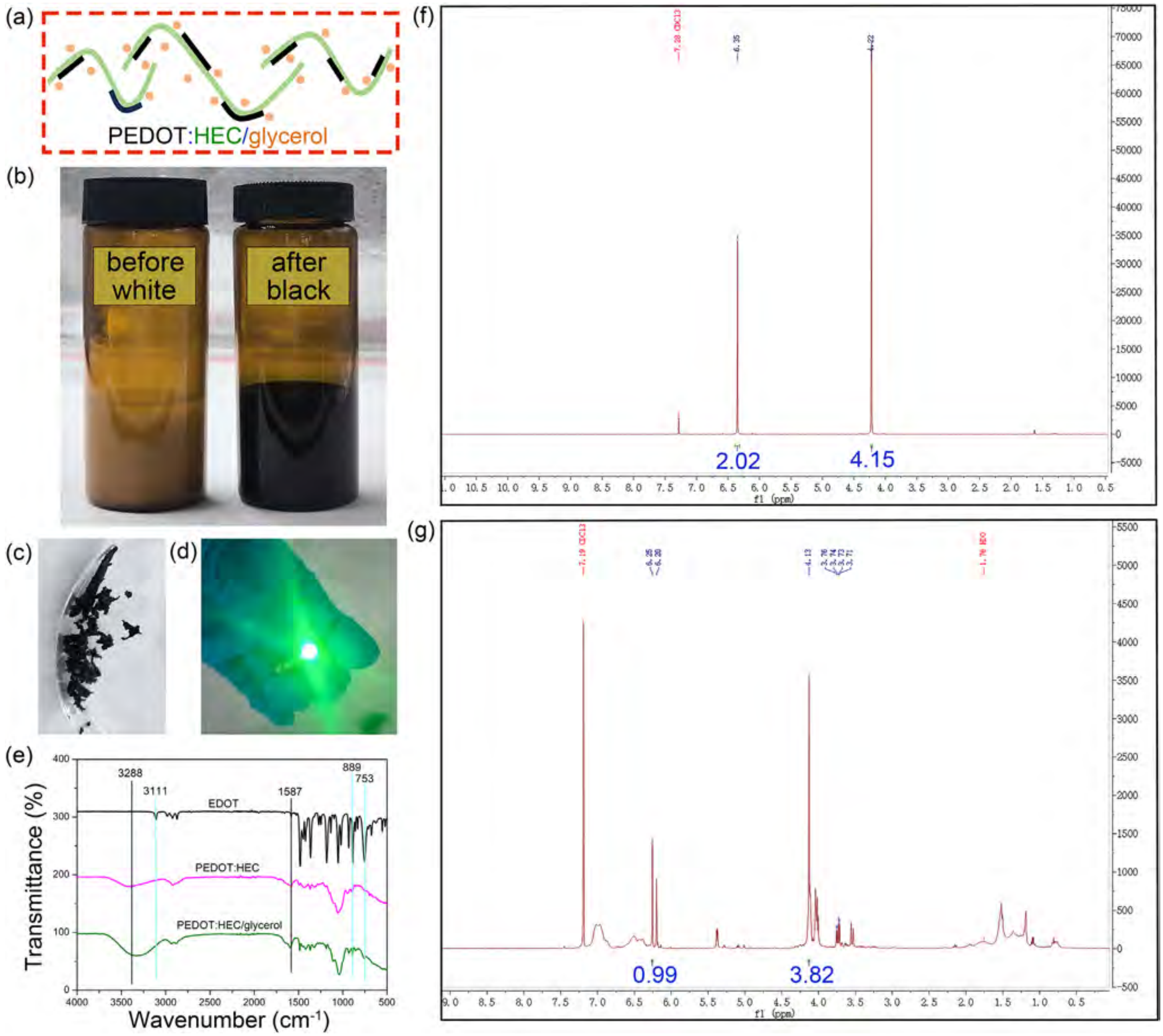

Figure 2. Structural and functional characterization of PEDOT:HEC/glycerol composites. a) Schematic of PEDOT:HEC/glycerol polymerization network. b) Visual transition during EDOT polymerization (monomer versus polymer states). c) The solid-state of PEDOT: HEC/glycerol polymer. d) Conductivity demonstration via dry-state circuit illumination. e) FTIR spectra of EDOT, PEDOT:HEC, and PEDOT: HEC/glycerol. f) ^{1}H-NMR spectrum of EDOT monomer. g) ^{1}H-NMR spectrum of PEDOT:HEC/glycerol polymer.

the winding roller, and subjected to a second electrospinning cycle. During this process, additional nanofibers are deposited onto the bundled yarns, resulting in a thicker suture with superior mechanical integrity. During the spinning process, ethyl alcohol increased the spinnability of the solution. The volatilization of ethyl alcohol accelerated the volatilization HFIP, resulting in faster formation of more stable nanofibers. Subsequently, the four sutures were placed in a fume hood to allow the residual ethyl alcohol and HFIP to completely evaporate. Finally, the four sutures were wetted with deionized water and then thermal crosslinking at 60 °C for 20 min. This crosslinking process was repeated several times until the nanofibers in the sutures did not detach under the force.

2.2. Polymerization of EDOT

Within HFIP, HEC functioned as a polymeric template, combining with EDOT through hydrogen bonding. This template effect enabled EDOT to polymerize in a certain direction and sequence, yielding a stable conductive PEDOT architecture. HEC simultaneously facilitated homogeneous PEDOT dispersion in HFIP, permitting successful electrospinning. Glycerol doping induced crystalline domain formation and PEDOT nanofiber interconnection (**Figure 2a**). Specifically, upon mixing optimized ratios of EDOT, HEC, and glycerol in HFIP, the system formed a milky suspension (Figure 2b, left). Subsequent polymerization converted EDOT to PEDOT, inducing a distinct chromatic transition to a jet-black conductive dispersion (Figure 2b, right), confirming successful π-conjugated network formation. Free-standing black polymer obtained upon solvent evaporation enabled dry-state conductive, as evidenced by bulb illumination (Figure 2c,d). This phenomenon confirmed both the successful polymerization of EDOT to PEDOT and charge carrier mobility, establishing the composite's efficacy as an electroactive biomaterial. From Figure 2e in the Fourier transform infrared spectroscopy (FTIR), the 1587 cm^{-1} peak corresponds to C—O—C skeletal vibrations in HEC. The peak at 3288 cm^{-1} was the O—H, which belonged to HEC and glycerol. Interestingly, the broadened O—H stretch indicated glycerol-enhanced H-bond networks. Furthermore, the peak of EDOT monomer at 3111cm^{-1} was attributed to the ≡C—H stretching vibration on the thiophene ring, which disappeared after polymerization. The peaks at 889 and 753 cm^{-1} were those usually associated with specific structures of EDOT, such as vibrations, and these peaks also diminished or disappeared after polymerization. From the proton nuclear magnetic resonance (^{1}H-NMR), H in EDOT changed from the original 4:2 to 4:1, indicating chain-growth polymerization efficacy (Figure 2f,g).

2.3. Characteristics of Sutures

The four sutures before thermal crosslinking are shown in **Figure 3a**, exhibiting a black surface color for PEDOT-containing sutures. Surface fibers on all sutures were within the nanometer range (Figure 3b,c). Cross-sectional scanning electron microscopy (SEM) analysis revealed a shell-core structure, comprising a nanofiber shell layer and a PLA micron yarn core (Figure 3d). Bulb illumination tests demonstrated that while the non-PEDOT's PGH suture failed to illuminate the bulb, the PEDOT-containing PGHE, PGHE-CS2, and PGHE-CS4 sutures all produced illumination (Figure 3e). The incorporation of non-conductive PLA within the fibers resulted in reduced bulb illumination intensity compared to the PEDOT: HEC/glycerol polymer shown in Figure 2d. Notably, conductivity was retained in the dry state despite PLA's attenuating effect on conductivity strength. However, the shell and core layers were unstable and easily separated from each other in the wet state, indicating that the nanofibers were not firmly bonded (Figure 3f).

After the sutures were thermal crosslinked, the color of the sutures was darker than that of the non-crosslinking sutures, and the suture diameter was 0.59 ± 0.13 mm, accompanied by slight fiber deformation while retaining their nanofiber structure (Figure 3g,i). In contrast to their pre-crosslinked state (Figure 3f), the thermally crosslinked sutures maintained structural integrity in the wet state, resisting shell-core layer separation under manual handling and forming a cohesive unit (Figure 3h). This demonstrates that thermal crosslinking significantly enhanced suture stability. Finally, the crosslinked suture was fitted with a compatible needle, rendering it suitable for general suturing applications (Figure 3j).

From **Figure 4a–c**, electrical characterization revealed that PGHE, PGHE-CS2, and PGHE-CS4 sutures exhibited conductivity in the dry state after thermal crosslinking (PGH was non-conductive, with resistivity exceeding instrument range, and thus omitted). Moreover, the conductivity of all three sutures improved in the wet state, demonstrating their excellent charge transport capability (Figure S1, Supporting Information). The mass loss of sutures after 8 weeks ranged from approximately 20% to 40%. This indicated that the degradation process had commenced and was proceeding steadily, with molecular decomposition occurring while the bulk structure remained intact to provide sustained mechanical support (Figure 4d). After 8 weeks of degradation, the conductivity of the sutures in the wet state decreased (Figure S2, Supporting Information), but remained within the effective range for ES mediated by biomaterials.[34–36] When the stress-strain curve of the four sutures showed a downward trend, surface nanofibers developed microcracks while the sutures maintained structural integrity without complete fracture. Notably, PEDOT-containing sutures displayed significantly enhanced mechanical strength (Figure 4e–i). This reinforcement mechanism primarily stems from EDOT polymerization, which strengthens intermolecular interactions between components. Furthermore, water contact angle measurements confirmed that HEC imparted hydrophilicity to the sutures, and the incorporation of PEDOT promoted greater exposure of hydroxyl groups from the HEC template on the suture surface, significantly increasing hydrogen bonding sites and substantially enhancing hydrophilicity. Consequently, PGHE, PGHE-CS2, and PGHE-CS4 demonstrated markedly superior hydrophilicity compared to PGH (Figure 4j,k). Collectively, these results demonstrate that the thermally crosslinked PEDOT-incorporated sutures exhibit stable electrical conductivity, controlled degradation, enhanced mechanical properties, and excellent hydrophilicity, meeting essential requirements for Achilles tendon sleeve avulsion repair applications.

2.4. Anti-Inflammatory Effect of CS

After culturing mouse mononuclear macrophages (RAW264.7) in the extraction solution for 4 days, the majority of cells in the PGH and PGHE groups were still round, while the cells in the CS groups showed vacuolation. After 7 days, some RAW264.7 in the PGH showed pseudopodia, potentially indicative of cellular polarization during culture. Although vacuolation in the CS groups was reduced, the number of cells in the CS groups was also lower than in the other groups (**Figure 5a**). RAW264.7 seeded on sutures was subjected to ES at 10 mV, 1 mA. Cell viability in the PGHE-CS2 and PGHE-CS4 was significantly lower than PGH and PGHE after 4 and 7 days, while no significant difference existed between the PGH and PGHE groups (Figure 5b). Live/dead staining at day 7 revealed pseudopodia formation in some cells within the PGH and PGHE groups, whereas PGHE-CS2 and PGHE-CS4 groups showed no pseudopodia formation and exhibited significantly fewer viable cells (Figure 5c). Corresponding SEM showed significantly fewer RAW264.7 adhering to nanofibers in PGHE-CS2 and PGHE-CS4 compared to the other two groups (Figure 5d). The above results showed that CS played a major role in affecting RAW264.7 in the presence of both ES and CS. CS reduced RAW264.7 viability while suppressing cellular polarization.

To assess the effect of CS on RAW264.7, the lipopolysaccharide (LPS)-induced macrophage polarization model was established by adding LPS to all groups except the control (Figure 5e). Flow cytometry analysis (Figure 5f,h) revealed a rightward shift in all

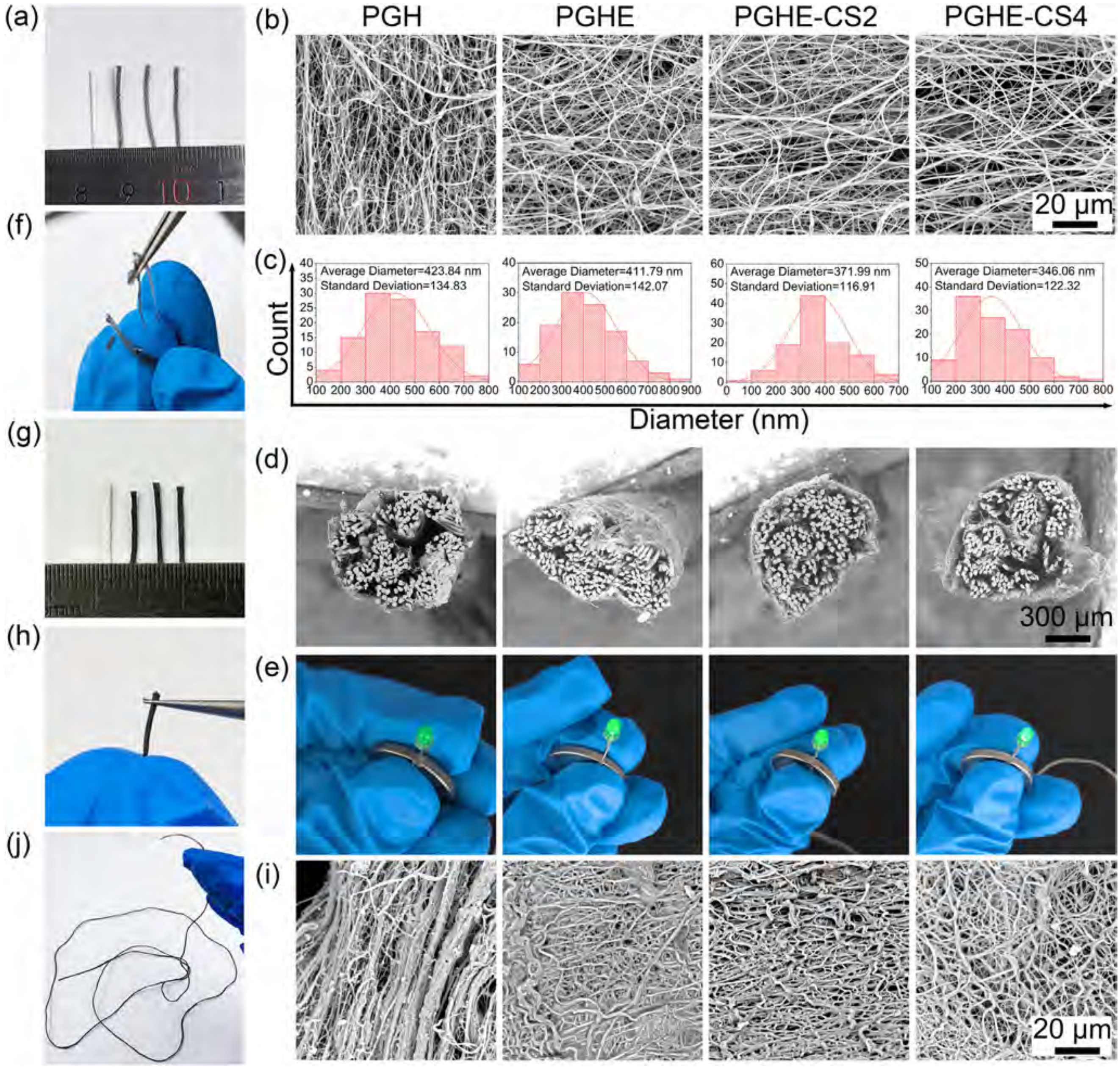

Figure 3. Characterization of sutures before and after thermal crosslinking. a) Macroscopic image in dry state (before crosslinking). b) SEM image of the surface (before crosslinking); scale bar = 20 µm. c) Corresponding nanofiber diameter statistics. d) SEM image of the cross-section (before crosslinking). e) Bulb illumination test in dry state (before crosslinking). f) Macroscopic image in wet state (before crosslinking). Macroscopic images after thermal crosslinking: g) dry state, h) wet state. i) SEM image of the surface (after crosslinking); scale bar = 20 µm. j) Overall macroscopic view of a suture with a needle (after crosslinking).

LPS-treated groups compared to the control, indicating that LPS successfully induced RAW264.7 polarization. Compared to the control+LPS group, the PGH, PGHE, PGHE-CS2, and PGHE-CS4 groups all exhibited varying degrees of leftward shift in CD80 and CD86 expression, indicating their regulatory effects on these markers. For CD80, there was no difference between PGH and PGHE, but these were significantly higher than PGHE-CS2 and PGHE-CS4, indicating that the presence of CS could more down-regulate the expression level of CD80 (Figure 5g). For CD86, the expression level of PGHE-CS4 was lowest (Figure 5i). Furthermore, qPCR analysis demonstrated that CS upregulated the expression of arginase-1 (ARG1) and interleukin-10 (IL-10) while downregulating interleukin-1β (IL-1β) and tumor necrosis factor-α (TNF-α) (Figure 5j-m). Collectively, these results indicated that the addition of CS had anti-inflammatory effects.

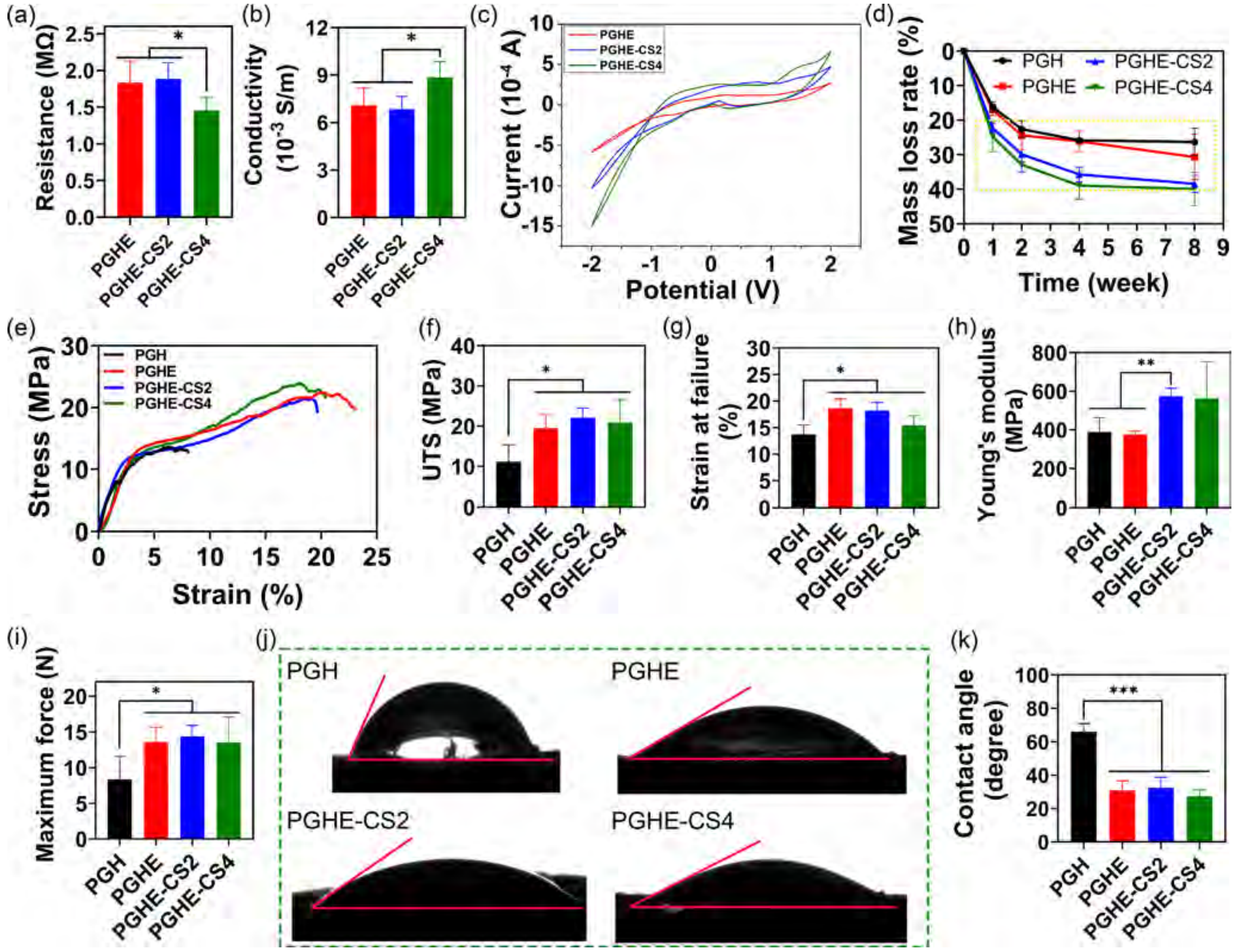

Figure 4. a) Resistivity, b) conductivity, and (c) cyclic voltammetry curves of the PGHE, PGHE-CS2, and PGHE-CS4 sutures in the dry state. d) The mass loss rate of sutures after 1, 2, 4, and 8 weeks of degradation. e) The stress-strain curve, f) ultimate tensile strength (UTS), g) strain at failure, h) Young's modulus, and i) maximum force of the sutures. j) Water contact angle test and k) corresponding angle statistics of the sutures. One-way analysis of variance followed by Tukey's post hoc test was used for statistical analysis. $^{*}p < 0.05$, $^{**}p < 0.01$, $^{***}p < 0.001$, $n \geq 3$.

2.5. In Vitro Tendon Regeneration Capability

Tenocytes were seeded onto sutures, and an ES model was established by applying 10 mV, 1 mA (**Figure** 6a). Under ES, cell viability in the PGHE, PGHE-CS2, and PGHE-CS4 groups was significantly higher than in both the PGH group and non-ES conditions, indicating that ES promoted tenocytes proliferation (Figure 6b). Furthermore, the PGHE-CS2 group exhibited the highest viability under ES after 4 and 7 days (Figure 6c). Live/dead staining revealed that most tenocytes on PGH sutures appeared punctate or aggregated. This morphology is likely attributable to the fibrous softness induced by HEC, which restricted cellular extension. Notably, the incorporation of PEDOT improved fiber texture, enabling tenocytes to extend a normal, spread morphology. Under ES, these cells also exhibited directional alignment (Figure 6d). SEM analysis confirmed superior cell spreading on PGHE, PGHE-CS2, and PGHE-CS4 fibers compared to PGH, with PGHE-CS2 supporting the most extensive spreading area (Figure 6e).

DAPI/collagen I (COL I) immunofluorescence (IF) staining revealed that the tenocytes number and COL I expression of PGHE were higher than PGH, indicating that ES was able to promote COL I expression. Notably, PGHE-CS2 exhibited superior COL I expression relative to both PGHE and PGHE-CS4, indicating that moderate CS concentrations optimize COL I production (Figure 6f–h). Similarly, DAPI/F-actin/ tenomodulin (TNMD) IF staining showed PGHE-CS2 achieved maximal cell number, spreading area, and TNMD expression among all groups (Figure 6i–l). Given the inhibitory effect of high CS concentration (PGHE-CS4) on tenocyte function, subsequent qPCR analysis excluded this group. Results confirmed that combined ES and moderate CS (PGHE-CS2) significantly upregulated tendon-associated genes fibromodulin (FMOD), COL I, and scleraxis (SCX) (Figure 6m–o). Collectively, these findings identify

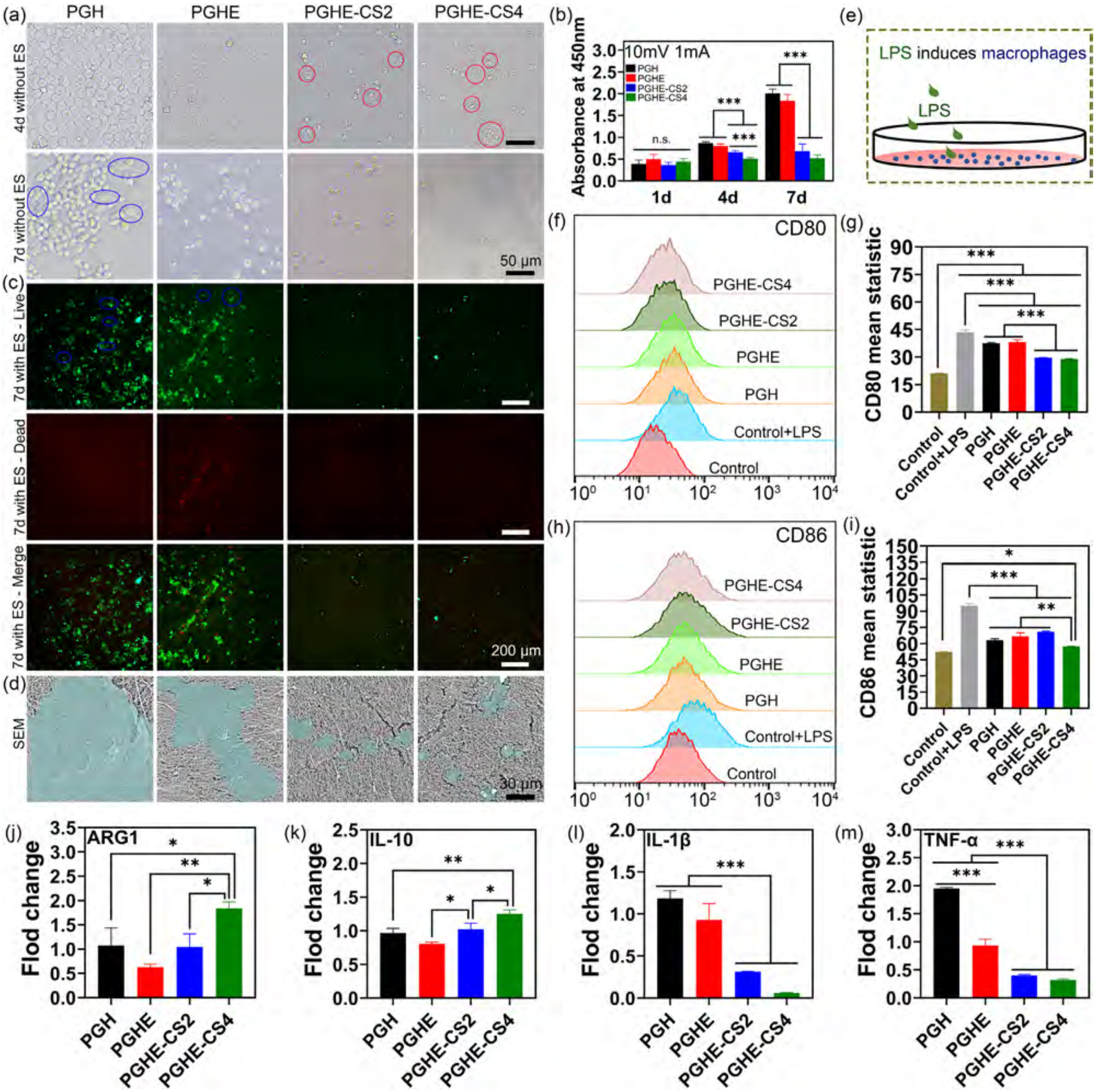

Figure 5. a) Morphology of RAW264.7 cultured in sutures extraction solution after 4 and 7 days, scale bar = 50 µm. b) Proliferation of RAW264.7 cultured on sutures for 1, 4, and 7 days under ES (10 mV, 1 mA). c) Live/dead staining and d) SEM of RAW264.7 cultured on sutures for 7 days with ES, scale bar = 200 µm, and scale bar = 30 µm, respectively. Blue circles: polarized cells, and red circles: vacuolated cells. e) Schematic diagram of LPS-induced RAW264.7 polarization to M1 phenotype, green: LPS, blue: RAW264.7, pink: culture medium. Flow cytometry analysis of f,g) CD80 and h,i) CD86 expression in LPS-induced RAW264.7. qPCR analysis of j) ARG1, k) IL-10, l) IL-1β, and m) TNF-α expression in LPS-induced RAW264.7. One-way analysis of variance followed by Tukey's post hoc test was used for statistical analysis. n.s.: no significance, $^*p < 0.05$, $^{**}p < 0.01$, $^{***}p < 0.001$, $n = 3$.

PGHE-CS2 as the optimal suture formulation for promoting tenocyte proliferation and tendon-marker expression.

2.6. In Vitro Osteogenic Ability

BMSCs were seeded onto sutures and subjected to ES. After 7 days of culture, the PGHE-CS2 group demonstrated optimal performance, significantly enhancing BMSCs proliferation and morphological extension across the fiber surface (**Figure** 7a–c). Specifically, BMSCs on PGH sutures exhibited rounded morphology with limited distribution, attributable to excessive fiber softness. In contrast, PEDOT-modified sutures (PGHE, PGHE-CS2, PGHE-CS4) displayed improved fiber texture, enabling extensive cell spreading with characteristic spindle morphology and intercellular connections (Figure 7a,c). The cell viability of PGHE

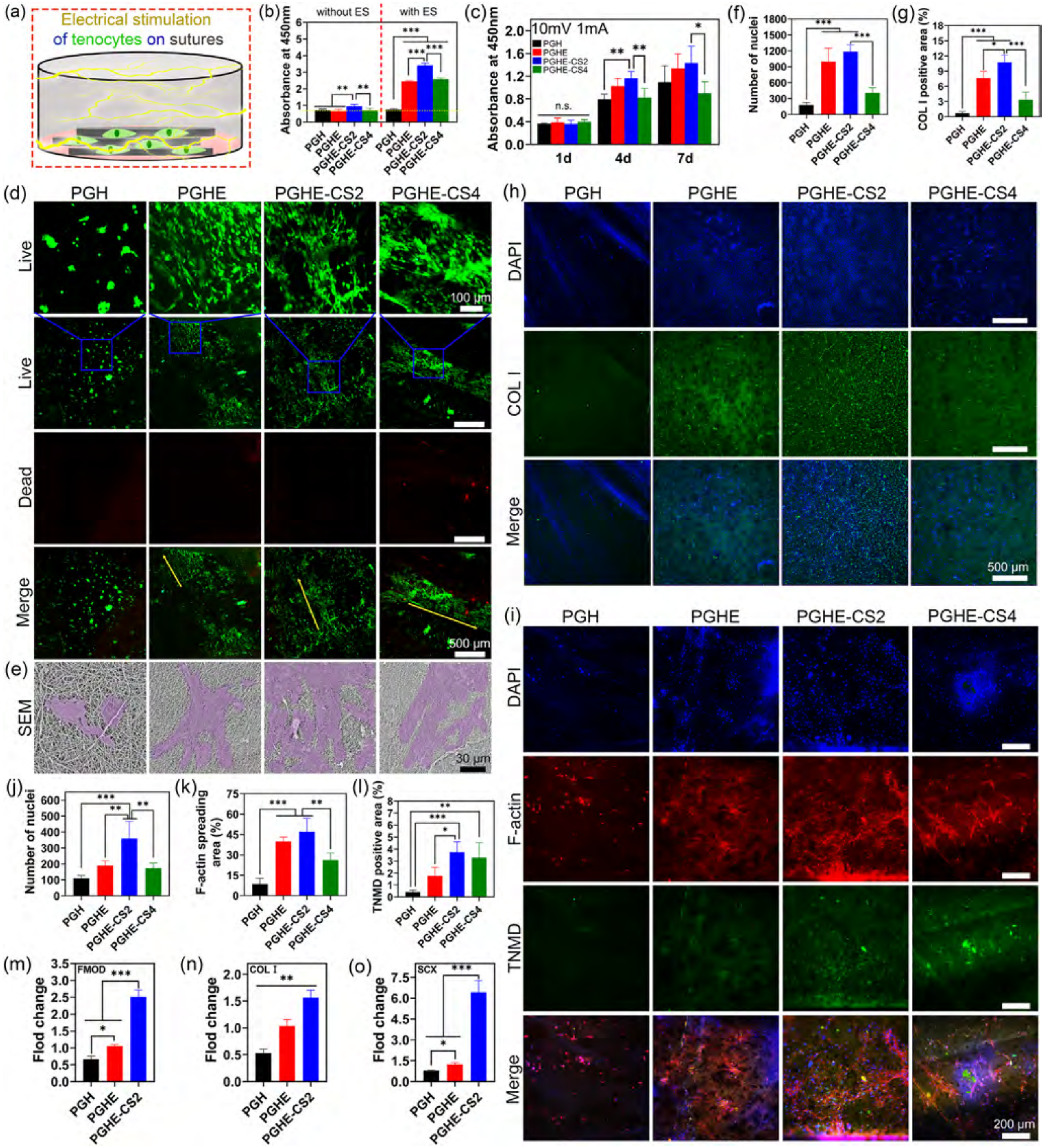

Figure 6. a) Schematic illustration of the ES experimental setup, yellow: ES (10 mV, 1 mA), green: tenocytes, black: sutures. b) Proliferation of tenocytes cultured on sutures without/with ES. c) Proliferation of tenocytes cultured on sutures for 1, 4, and 7 days under ES. d) Live/dead staining, and e) SEM morphology of tenocytes cultured on sutures after 7 days with ES, scale bar = 100 μm, scale bar = 500 μm, and scale bar = 30 μm, respectively. In vitro COL I expression of tenocytes cultured in sutures with ES after 14 days: f) Nuclei count quantification, g) COL I positive area analysis, and h) Representative DAPI/COL I IF staining, scale bar = 500 μm. In vitro TNMD expression of tenocytes cultured in sutures with ES after 14 days: i) Representative DAPI/F-actin/TNMD staining, scale bar = 200 μm, and j) nuclei count quantification, k) F-actin spreading area analysis, l) TNMD positive area analysis. qPCR analysis of tenocytes gene expression after 14 days with ES: m) FMOD, n) COL I, o) SCX. One-way analysis of variance followed by Tukey's post hoc test was used for statistical analysis. n.s.: no significance, *$p < 0.05$, **$p < 0.01$, ***$p < 0.001$, $n = 3$.

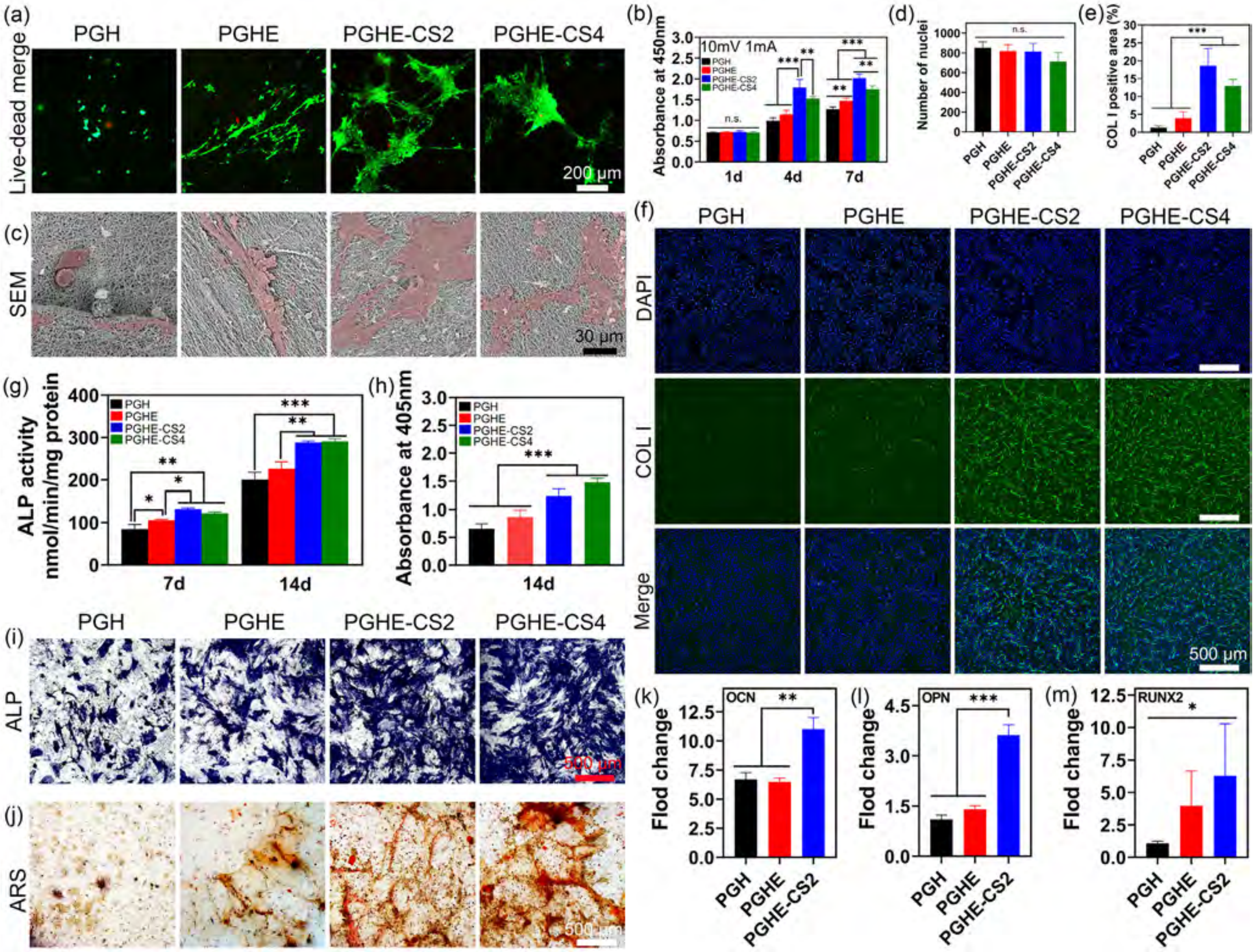

Figure 7. a) Live/dead staining of BMSCs cultured on sutures with ES (10 mV, 1 mA) after 7 days, scale bar = 200 μm. b) Proliferation of BMSCs cultured on sutures with ES after 1, 4, and 7 days. c) SEM morphology of BMSCs on sutures with ES after 7 days, scale bar = 30 μm. In vitro COL I expression of BMSCs cultured in bone-induced suture extraction solution with ES after 14 days: the statistics of d) nuclei quantification, e) COL I positive area, and f) DAPI/ COL I IF staining, scale bar = 500 μm. Osteogenic marker analysis of BMSCs cultured in bone-induced suture extraction solution with ES: g) ALP activity after 7 and 14 days, h) ARS activity after 14 days, i) Representative ALP staining and j) ARS staining after 14 days, scale bar = 500 μm. qPCR analysis of osteogenic gene expression of BMSCs cultured in bone-induced suture extraction solution with ES after 14 days: k) OCN, l) OPN, m) RUNX2. One-way analysis of variance followed by Tukey's post hoc test was used for statistical analysis. n.s.: no significance, *$p < 0.05$, **$p < 0.01$, ***$p < 0.001$, $n = 3$.

was significantly higher than PGH, while PGHE-CS2 further outperformed both PGHE and PGHE-CS4 (Figure 7b). The above demonstrated that ES and optimal CS loading synergistically promoted the proliferation and spreading of BMSCs, which had a similar effect as tenocytes.

IF staining analysis of DAPI/COL I in BMSCs revealed COL I elevated expression in both PGHE-CS2 and PGHE-CS4 (Figure 7d–f). In addition, the Alkaline phosphatase (ALP) and Alizarin Red S (ARS) expression ability of PGHE-CS2 and PGHE-CS4 were comparable and superior to the other two groups, indicating that the addition of CS could accelerate the osteogenic ability of BMSCs (Figure 7g–j). Notably, PGHE-CS4 could slow down the proliferation of BMSCs, and its osteogenic performance did not exceed PGHE-CS2 despite higher CS loading, indicating dosage limitations. Therefore, PGH, PGHE, and PGHE-CS2 continued for further qPCR to verify the osteogenic ability of BMSCs. The results showed that optimal CS concentration (PGHE-CS2) significantly upregulated osteogenic markers osteocalcin (OCN), osteopontin (OPN), and runt-related transcription factor 2 (RUNX2) of BMSCs in vitro. Importantly, the RUNX2 expression of PGHE was higher than PGH, indicating that ES was conducive to the accelerated expression of RUNX2 (Figure 7k–m). In other words, PGHE-CS2 emerges as the optimal formulation, synergistically promoting BMSCs proliferation and osteogenesis.

2.7. Reconstruction of the Achilles Tendon Sleeve Avulsion

Following the tendon was reattached to the bone, PGH showed significant inflammation that persisted throughout 12 weeks

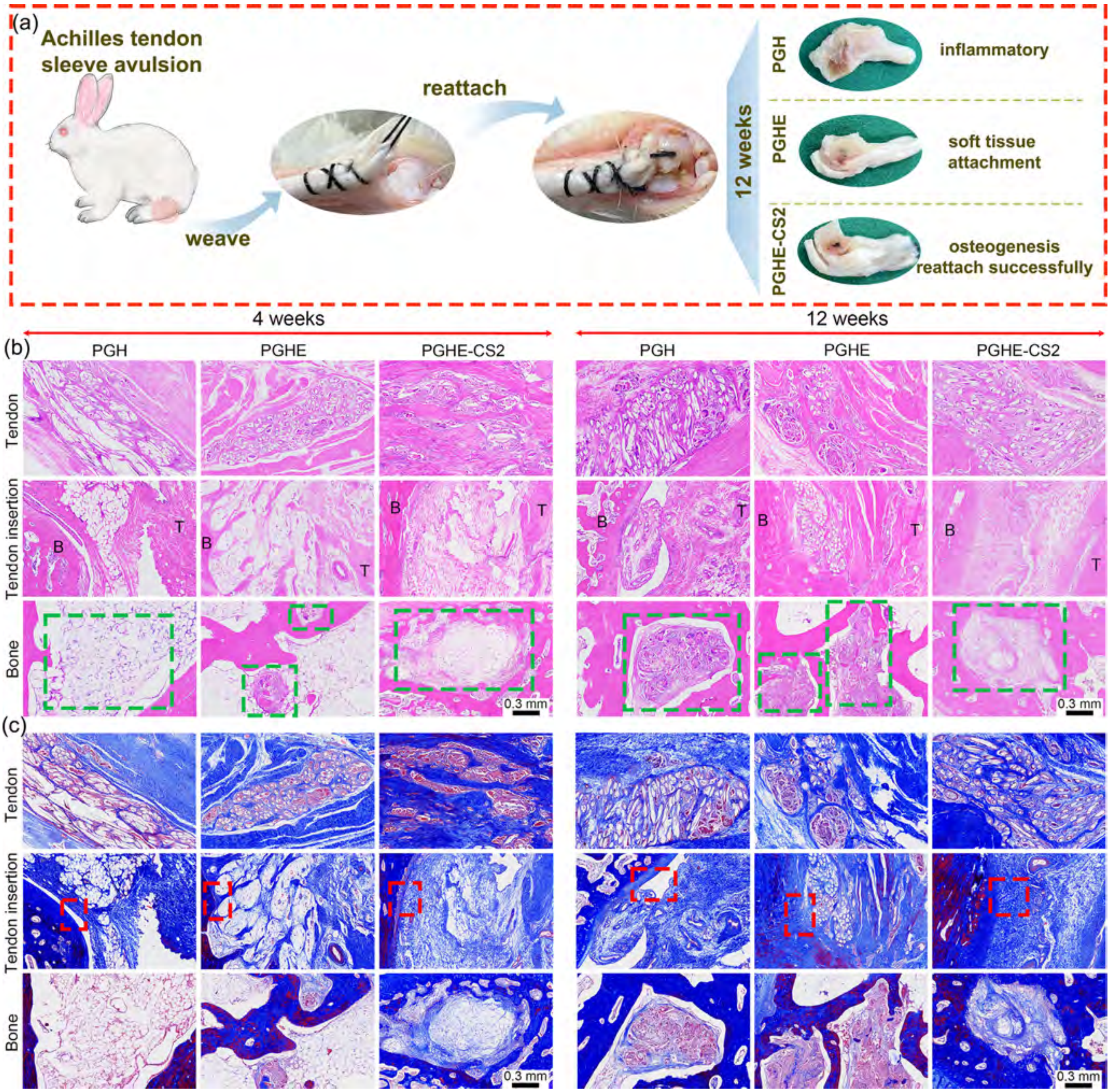

Figure 8. a) Macroscopic view of reconstructed Achilles tendon sleeve avulsion. b) HE staining and c) MT staining after 4 and 12 weeks post-operation, scale bar = 0.3 mm. Green box: bone tunnel. Red box: tendon insertion. B: bone. T: tendon.

with tissue remodeling. Meanwhile, new soft and hard tissues emerged around PGHE and PGHE-CS2 sutures, and the inflammatory response was relatively mild (**Figure 8a**).

From hematoxylin-eosin (HE) staining (Figure 8b), the newly formed tendon tissue had tightly adhered to the suture after 12 weeks. However, the PGH group exhibited progressively intensified inflammation, while PGHE-CS2 showed significantly reduced inflammatory infiltration compared to the other two groups. This could also lead to similar conclusions in tendon insertion and bone. In addition, there was a gap between the regenerated tissue of the PGH and the surrounding bone in the bone tunnel after 12 weeks, indicating that the bonding between the PGH suture and the surrounding bone was not firm. PGHE exhibited partial tissue-bone contact with residual gaps, while PGHE-CS2 achieved seamless integration, demonstrating that electroactive-CS dual functionalization enhances suture stability in the bone tunnel.

Masson's trichrome (MT) staining further showed unstable tendon insertion with minimal collagen in PGH, whereas PGHE and PGHE-CS2 displayed reduced gaps with observable collagen deposition at insertion sites (Figure 8c). Critically, PGHE-CS2 demonstrated superior collagen expression

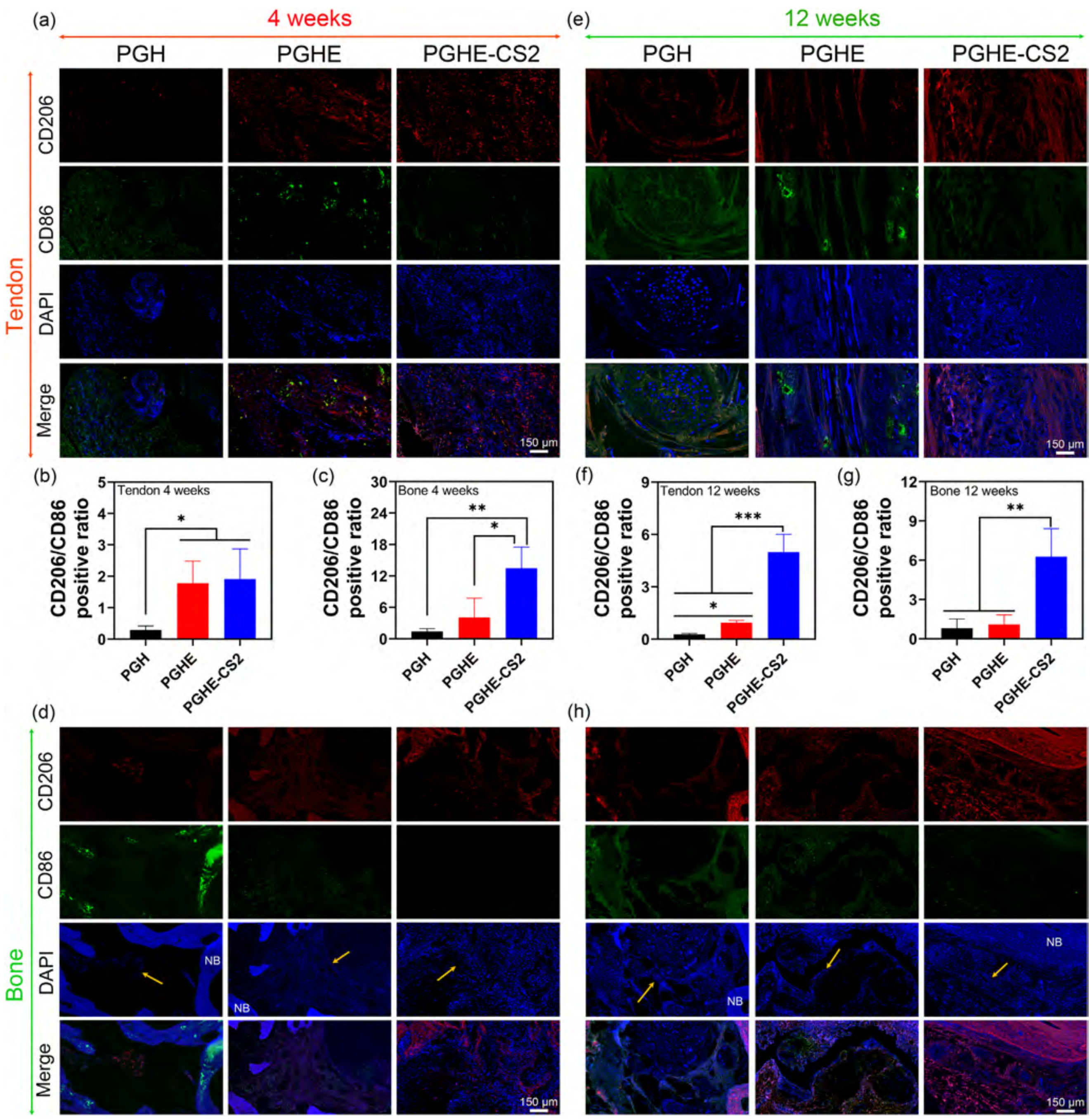

Figure 9. a–d) IF staining of CD206/CD86/DAPI and CD206/CD86 positive ratio of the newly formed tissue after 4 weeks post-implantation. e–h) Corresponding IF staining and positive ratio after 12 weeks. Scale bar = 150 µm. NB: native bone. Yellow arrow: the newly formed tissue in the bone tunnel. One-way analysis of variance followed by Tukey's post hoc test was used for statistical analysis. $^{*}p < 0.05$, $^{**}p < 0.01$, $^{***}p < 0.001$, $n = 3$.

across both tendon and bone tissues (Figure S3, Supporting Information).

To further assess the inflammation in the regenerated tendon and bone tissue, IF staining of CD206 and CD86 was performed at 4 and 12 weeks post-implantation. In tendon tissue at 4 weeks, PGH exhibited intense inflammation with minimal CD206 expression, while PGHE and PGHE-CS2 showed elevated CD206 levels (**Figure** 9a,b). By 12 weeks, with tissue remodeling and suture degradation, PGH maintained persistent inflammation with a low CD206/CD86 ratio. PGHE-CS2 demonstrated significantly higher CD206 expression and optimal anti-inflammatory capacity (Figure 9e,f).

For bone tissue, there were slight differences from tendon tissue. In the bone tunnel after 4 weeks, the number of DAPI in PGH was small, indicating that there was very little new tissue. Conversely, there were more new tissues and higher positive expression of CD206 in PGHE-CS2 (Figure 9c,d). After 12 weeks, the levels of CD86 in PGH and PGHE were upregulated, accompanied by an increase in the expression of CD206. However, the positive ratio of CD206/CD86 was generally lower than that of PGHE-CS2 (Figure 9g,h). The above indicates that PGHE-CS2 had a higher anti-inflammatory ability than the other two groups.

Immunohistochemistry (IHC) staining revealed that all groups showed positive expression of COL I and FMOD in tendon tissue, but the expression levels varied among groups. Among them, PGHE and PGHE-CS2 demonstrated markedly higher expression than PGH (**Figure** 10a–c). In our previous research,[37] we found that conductive materials could promote FMOD expression and enhance glycosaminoglycan binding protein pathways. In this study, we further introduced new conductive materials and the glycosaminoglycan of CS, which were similarly validated to promote tendon tissue regeneration. In bone tunnels, PGHE significantly outperformed PGH in COL I and OCN expression, while PGHE-CS2 surpassed both groups, confirming PGHE-CS2's superior capacity to enhance osteogenesis (Figure 10d–f).

3. Discussion

Achilles tendon sleeve avulsion represents a clinically intractable condition due to the absence of viable tissue for direct reattachment at the insertion site.[38] The native bioelectrical signal that is critical to tendon function is disrupted.[39] Furthermore, conventional non-absorbable sutures risk permanent retention with associated complications, including chronic inflammation, infection, and foreign body reactions.[40] To address these limitations, we engineered a multifunctional surgical suture featuring electroactivity, biodegradability, anti-inflammatory properties, and regenerative capacity for tendon-to-bone integration (Figure 1).

Our material innovation leverages HEC to disperse EDOT monomers, enabling polymerization into PEDOT within HFIP solvent systems. This approach circumvents the aqueous dispersion limitations inherent to PSS-dependent methodologies, significantly expanding PEDOT's biomedical applicability (Figure 2b). Continuous agitation under controlled heating facilitated catalyst-free EDOT polymerization (Figure 2e–g). In addition, the glycerol incorporation enhanced the conductivity of PEDOT (Figure 2d). Compared to the rough shell layer of yarns obtained by electrospun in the past, the surface fibers obtained by adding glycerol to this suture were softer, which was beneficial for tissue suturing and traction, greatly improving comfort in bone tunnels. Critically, the strategic addition of ethyl alcohol accelerated HFIP volatilization during spinning, stabilizing fiber ejection kinetics without compromising PEDOT conductivity (Figures 3e and 4b). Subsequent thermal crosslinking yielded structurally stable sutures suitable for repairing Achilles tendon sleeve avulsion (Figure 3j).

Current commercial sutures exhibit mechanical strength profiles incompatible with osseous stress environments, leading to suture micromotion within bone tunnels that progressively widen the bone tunnel over time.[41] This instability is compounded in patients with comorbidities, where tendon weakening, muscular atrophy, and restricted joint mobility following primary repair often precipitate failure of conventional sutures and tendon substitutes.[42] Furthermore, non-degradable materials occupy space in the bone tunnel indefinitely without inducing osteogenesis,[43] collectively exacerbating tendon-bone bonding failure. Our suture strategically addresses these limitations through: i) Core reinforcement via multiple PLA micron yarn strands, ensuring the core strength of the suture (Figure 3d). ii) Surface stabilization through hydrogen-bonded PEDOT networks that significantly enhance mechanical strength compared to those without PEDOT (Figure 4e,i). iii) Robust fiber fixation is achieved by thermal crosslinking, which maintains structural integrity under a forceful and moist environment (Figures 3h and 8a). It could be seen that there was a match between this suture and the bone tunnel. (iv) IHC analysis confirmed that the synergistic effects of electroactive polymers and CS in PGHE-CS2 sutures accelerated the formation of tendon and bone tissues, which was beneficial to the stability of tendon re-fixation on the bone (Figure 10). This regenerative capability, absent in commercial sutures, directly addresses the fundamental instability underlying repair failures.

As a negatively charged glycosaminoglycan, CS functions as a dopant or charge carrier when incorporated into the PEDOT/HEC/glycerol/PLA nanofibrous shell. Elevated CS concentration (PGHE-CS4) increased mobile ions or charge traps within the material, thereby significantly enhancing suture conductivity (Figure 4b). Concurrently, CS exerts dose-dependent anti-inflammatory effects by suppressing pro-inflammatory cytokines, promoting anti-inflammatory factors, and modulating macrophage polarization. As demonstrated in Figure 5, high-CS (PGHE-CS4) potently reduced RAW264.7 viability, inhibited pseudopodia formation, downregulated CD80/CD86, and optimized inflammatory factor expression. Although CS is widely recognized to facilitate bone and tendon formation, elevated CS concentrations coupled with high conductivity do not necessarily enhance the proliferation or differentiation of tenocytes and BMSCs. This was observed that PGHE-CS4 unexpectedly impaired cellular proliferation and differentiation compared to PGHE-CS2 under identical ES conditions (Figures 6 and 7). This is mainly due to: 1) Tissue regeneration requires moderate inflammatory signals to initiate repair cascades, which may be overly suppressed by high-CS anti-inflammatory potency. 2) Excessive CS release could saturate receptors or trigger negative feedback, while an altered material microenvironment (surface charge/topography) further compromises cellular responses. In contrast, PGHE-CS2 optimally balanced conductivity (Figure 4b), anti-inflammation (Figures 5 and 9), and pro-regenerative functions. By harmonizing electroactivity and CS bioactivity, PGHE-CS2 maximized expression of key markers (Figures 6 and 7), ultimately achieving superior tendon-bone integration and anti-inflammatory outcomes in vivo (Figures 8–10). This underscores the critical importance of dose balancing in multifunctional biomaterial design.

Ane et al.[44] demonstrated that replacing PEDOT:PSS with PEDOT nanoparticles (NPs) eliminates the issue of PSS residue. Cells proliferated well on silk fibroin conduits incorporated with 1-10% PEDOT NPs, confirming the non-cytotoxicity of this composite conduit. Manuel et al.[45] utilized hematin to catalyze the copolymerization of EDOT and pyrrole (Py), circumventing the toxicity associated with residues from conventional oxi-

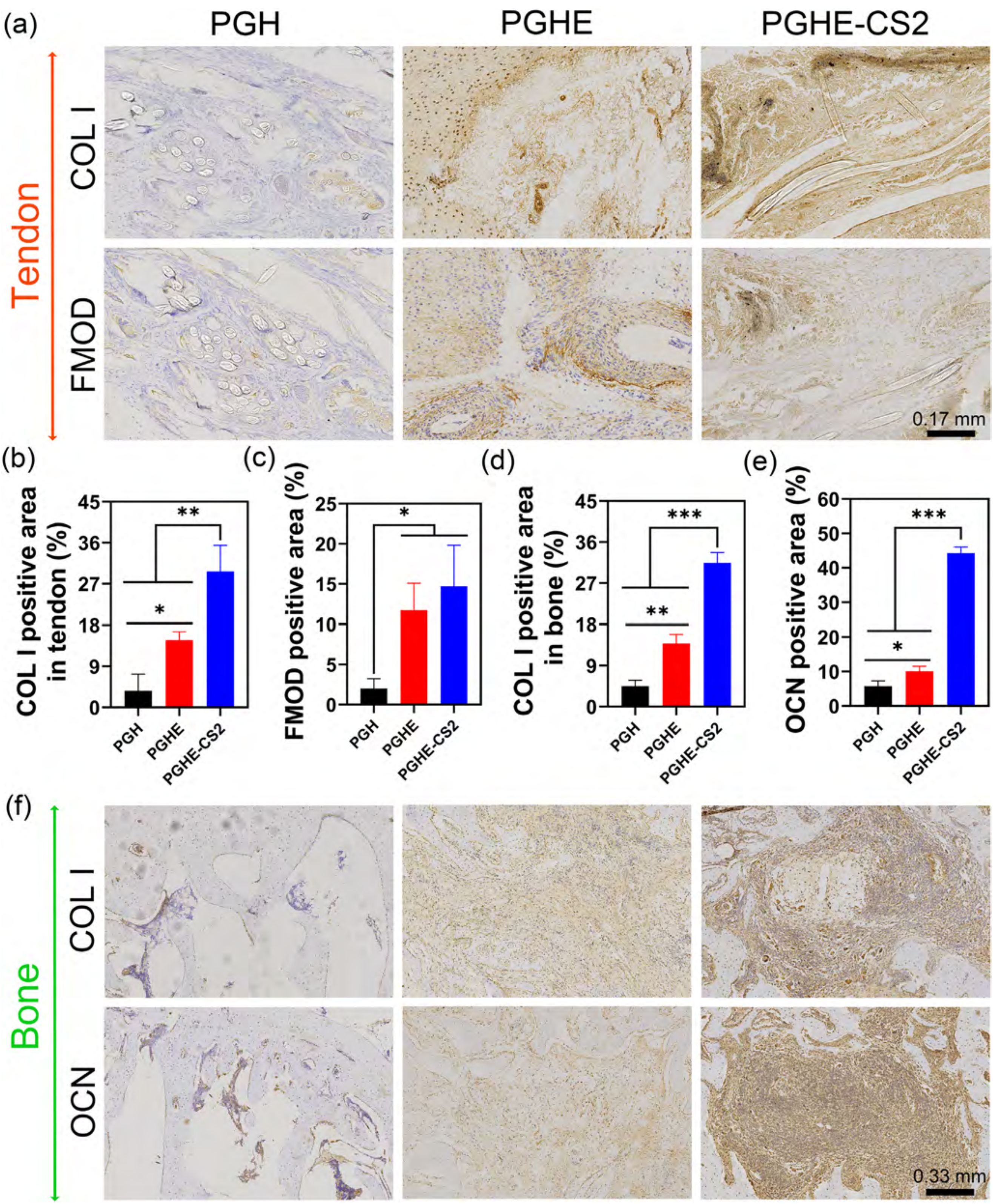

Figure 10. a) Representative IHC staining of COL I and FMOD in tendon tissue, scale bar = 0.17 mm. b,c) Quantitative analysis of COL I and FMOD expression in the tendon. d,e) Quantitative analysis of COL I and OCN expression in bone tissue. f) Representative IHC staining of COL I and OCN in bone, scale bar = 0.33 mm. One-way analysis of variance followed by Tukey's post hoc test was used for statistical analysis. $^{*}p < 0.05$, $^{**}p < 0.01$, $^{***}p < 0.001$, $n = 3$.

dants. No toxic effects were observed in either paramecium or mammalian cell experiments at EDOT-Py particle concentrations $\leq$1 mg mL^{-1}. Notably, paramecium cells exhibited 100% survival and normal excretory function after internalizing EDOT-Py particles at 10 μg mL^{-1}, with complete excretion occurring within 72 h. Collectively, these studies indicate that EDOT/PEDOT at low doses exhibits negligible intrinsic toxicity, and its potential toxicity can be effectively mitigated through material design (nanoparticle formulation, biocompatible carrier encapsulation) and green synthesis strategies (biomimetic catalysis). This is corroborated by our findings: PGHE-CS2 sutures, synthesized via the green polymerization of EDOT using an HEC/glycerol system, were non-toxic to tenocytes and BMSCs and promoted their proliferation (Figures 6c,d, and 7a,b). Furthermore, Jia's team[46] developed a degradable PEDOT-COOH polymer for implantable zinc batteries. Its degradation products promoted cell growth at concentrations <60 μg mL^{-1}. The material completely disappeared 8 weeks after subcutaneous implantation in SD rats, and HE staining revealed no inflammation or lesions in major organs, demonstrating complete biodegradation and excellent biocompatibility of the degradation products. Similarly, our PGHE-CS2 sutures implanted in rabbits for 12 weeks showed no mortality attributable to potential PEDOT toxicity. HE and IF staining indicated low levels of inflammation in tendon and bone tissues (Figures 8b and 9). Therefore, under the described experimental conditions, the inherent toxicity of low-dose PEDOT materials and their degradation byproducts toward tenocytes, BMSCs, and in vivo animal models is negligible.

Critically, to assess the functional persistence of the conductive network during the key healing phase, we monitored the conductivity of PGHE, PGHE-CS2, and PGHE-CS4 sutures under in vitro degradation conditions. In physiological wet environments, water molecules penetrate the PEDOT/HEC conductive network, acting as ion transport media that enhance charge mobility. This hydration effect increased conductivity by approximately 30-fold compared to the dry state (Figure 4b; Figure S1, Supporting Information). Notably, while conductivity gradually decreased with suture degradation, all remained within the effective range for conductive biomaterials (Figure S2, Supporting Information). This controlled electroactivity aligns with established timelines for active tendon-bone healing and remodeling,[47] ensuring the suture delivers essential bioelectrical signals during initial healing stages to modulate cellular behaviors (proliferation, migration, differentiation) and then gives way to regenerated tissue. Therefore, these sutures are a promising platform for electrically responsive tissue regeneration. Nevertheless, ultra-long-term applications of PEDOT-based implants warrant deeper investigation into degradation kinetics, accumulation effects of degradation products, and potential chronic impacts.

The innovative aspects and limitations of this study are inherently complementary. Through systematic variation of component ratios, we determined the optimal formulation: 0.25 g PLA, 0.5 g glycerol, 0.5 g EDOT, and 0.5 g HEC dissolved in 16 mL HFIP. Reducing PLA content impaired spinnability, while increasing it yielded non-conductive fibers. This indicates that polymers like PLA are substitutable, though replacement necessitates re-optimization of polymer dosage. Similarly, decreasing EDOT or HEC compromised fiber conductivity. The viscosity imparted by HEC mandated a minimum of 16 mL HFIP; further dilution with HFIP impaired spinnability. To address this, we strategically introduced ethyl alcohol as a spinning aid. Crucially, our approach innovatively achieved in situ synthesis of conductive PEDOT solely through the synergistic environment provided by HEC, glycerol, and HFIP, leveraging hydrogen bonding between components. This method represents an environmentally benign route to PEDOT formation. The conductivity of the PEDOT synthesized through this method was relatively lower than commercially available alternatives. Nevertheless, with our current components, the fibers maintained measurable conductivity even after months of storage in a drying oven. This electroactivity stability confirms their suitability for in vivo applications.

4. Conclusion

This study developed a novel biomaterial platform addressing the critical limitations of conventional, biologically inert sutures used in Achilles tendon sleeve avulsion repair. The key comparative advantage of this multifunctional suture lies in its dual functionality: inherent electroactivity and potent anti-inflammatory modulation, achieved through solvent-mediated synthesis and an electrospinning strategy. Leveraging the HEC/glycerol/HFIP system enabled eco-friendly in situ PEDOT polymerization, establishing a conductive framework. Compared to current clinical options, this suture actively promotes tissue regeneration by restoring the disrupted bioelectrical microenvironment essential for healing. In vitro, the incorporated CS significantly downregulated pro-inflammatory cytokines, effectively countering the chronic inflammation often associated with traditional non-degradable implants, while the synergy between electroactivity and CS robustly enhanced tenocytes and BMSCs proliferation and differentiation under ES. In vivo, the suture successfully reattached ruptured tendons to the calcaneus. Critically, at 12 weeks post-operation, attenuated inflammation coupled with robust new tissue formation enhanced tendon-bone integration and bone tunnel stability, thereby achieving functional reconstruction through coordinated material degradation and biological regeneration, offering a promising advanced solution beyond mere mechanical fixation.

5. Experimental Section

Materials: Polylactic acid micron yarn (PLA micron yarn) was from Shanghai Taixin New Material Technology Co., Ltd. Polylactic acid (PLA, Mw = 110000) was from RHAWN Reagent. Glycerol (99%, MW = 92.09) was from Shanghai Aladdin Biochemical Technology Co., Ltd. Hydroxyethyl cellulose (HEC, 5000 - 6400 mpa.s) was from Shanghai Meryer Biochemical Technology Co., LTD. 3,4-ethylenedioxythiophene (EDOT, 99%+, MW = 142.18) was from Adamas-beta. Chondroitin sulfate (CS, 95%) was from Shanghai Bide Pharmatech Co., Ltd. Ethyl alcohol ($\geq$99.9%) was from Sinopharm Chemical Reagent Co., Ltd. Hexafluoroisopropanol (HFIP, $\geq$99.5%, MW = 168.04) was from Shanghai Darui Fine Chemicals Co., LTD.

Characterization of EDOT Polymerized to PEDOT: EDOT, HEC, and glycerol were dissolved in HFIP following the prescribed protocol under constant stirring. Solution color evolution was quantitatively monitored until stabilization. Upon reaching chromatic equilibrium, the solution was solvent-cast in a fume hood and dried to obtain solid-state polymer composites. Dry-state electrical conductivity was qualitatively assessed using an LED circuit: illumination confirmed current generation. Fourier transform infrared spectroscopy (FTIR) and proton nuclear magnetic resonance

(^{1}H-NMR) analyses were employed to verify EDOT polymerization into PEDOT and characterize molecular structure.

Characterization of Suture: The characterization of the PGH, PGHE, PGHE-CS2, and PGHE-CS4 sutures includes scanning electron microscopy (SEM), LED circuit, multimeter measurement of resistance, cyclic voltammetry tests, mass degradation, mechanical tensile, and water contact angle. A description of the experimental details is in the Supporting Information.

In Vitro Anti-inflammatory Ability: RAW264.7 was obtained from Wuhan Saiweier Biotechnology Co., Ltd. To evaluate the combinatorial effects of CS and ES (based on previous studies,[37] all ES parameters were set to 10 mV, 1 mA) on RAW264.7 behavior, the cellular morphology, proliferation, live/dead staining, and adhesion were tested. Additionally, macrophage polarization was induced by lipopolysaccharide (LPS, 100 ng mL^{-1}). The CD80 and CD86 expression of RAW264.7 was analyzed by a Flow cytometer. The anti-inflammatory effect of CS was further validated through qPCR analysis of inflammatory gene expression (primer sequences: Table S1, Supporting Information). Comprehensive experimental protocols are detailed in the Supporting Information.

In Vitro Tenocytes Biocompatibility and Expression: Tenocytes were isolated from 2-week-old Sprague Dawley (SD) rats (Shanghai Jiesijie Laboratory Animal Co., Ltd.) using established protocols.[48] To evaluate the effects of ES on tenocyte-suture interactions, an in vitro ES model was implemented. Cellular responses were assessed through proliferation, live/dead staining, and adhesion. Additionally, immunofluorescence (IF) staining of tendon-specific markers (collagen I, COL I; tenomodulin, TNMD) quantified the ability of sutures to induce tendon regeneration in vitro. Gene expression was further analyzed via qPCR (primer sequences: Table S2, Supporting Information). The comprehensive methodology is detailed in Supporting Information.

In Vitro BMSCs Biocompatibility and Osteogenic Potential: BMSCs were isolated from 2-week-old SD rats according to the previous method.[49] The biocompatibility of the suture to the BMSCs was verified by proliferation, live/dead staining, and adhesion. In addition, the COL I IF staining, Alkaline phosphatase (ALP) activity, and Alizarin Red S (ARS) staining of BMSCs verified the osteogenic ability of sutures in vitro. Finally, the qPCR was also used to investigate BMSCs osteogenic expression (primer sequences: Table S3, Supporting Information). A description of the experimental details is in the Supporting Information.

In Vivo Repair of Achilles Tendon Sleeve Avulsion in Rabbit: This study passed the ethical approval of Chedun Experimental Animal Breeding Farm Co., LTD., Songjiang, Shanghai (2024102215). An Achilles tendon sleeve avulsion model was established in adult New Zealand White rabbits to evaluate the efficacy of PGH, PGHE, and PGHE-CS2 sutures in tendon weaving, traction, and fixation. After anesthesia induction with Zoletil 50 (tiletamine-zolazepam, 7 mg kg^{-1}) via auricular vein injection, the posterolateral hindlimb was shaved and aseptically prepared with povidone-iodine and 75% ethyl alcohol. A longitudinal incision exposed the calcaneus and Achilles tendon insertion. Complete tendon detachment from the calcaneal insertion was achieved via sharp dissection to create the sleeve avulsion defect. A transverse bone tunnel (1.5 mm diameter) was drilled through the calcaneus using a Kirschner needle. Sterile sutures (PGH, PGHE, and PGHE-CS2) armed with taper-point needles were woven through the ruptured tendon ends. The suture was then passed through the bone tunnel, fixing the tendon to its anatomical insertion under tension. Following knot fixation over the calcaneal bridge, the suture ends were redirected into the tendon substance for secondary fixation. The wound was closed in layers and dressed with povidone-iodine. The postoperative antibiotic was administered for 72 h. The mental and activity conditions of the rabbits were observed regularly.

Histological Analysis: At 4- and 12-week endpoints, animals were euthanized. The tendon-bone complexes were harvested, fixed in 4% paraformaldehyde, and decalcified in 14% EDTA. Serial sections underwent: hematoxylin-eosin (HE) staining, Masson's trichrome (MT) staining, IF staining, and immunohistochemistry (IHC) staining.

Statistical Analysis: All experiments were performed with a minimum of three independent replicates per sample group. All data were expressed as mean ± standard deviation. One-way analysis of variance followed by Tukey's post hoc test was used for statistical analysis. The significant difference was considered at $^{*}p < 0.05$ and $^{**}p < 0.01$, $^{***}p < 0.001$ (GraphPad Prism 8.0 software, USA).

Supporting Information

Supporting Information is available from the Wiley Online Library or from the author.

Acknowledgements

X.Y. and C.L. contributed equally to this work. This work was supported by the Fundamental Research Funds for the Central Universities (2232023D-10) and Zhongshan Traditional Chinese Medicine Inheritance and Innovation Development Research Program (No. 2024B3020). This work was supported by the National Natural Science Foundation of China (No. 82202685) and the First Affiliated Hospital of Zhengzhou University (LHGJ20220355). This work was supported by the Science and Technology Commission of Shanghai Municipality, China (20DZ2254900), Sino-German Science Foundation Research Exchange Center, China (M-0263). This project was also supported by Ongoing Research Funding program (ORF-2025-769), King Saud University, Riyadh, Saudi Arabia

Conflict of Interest

The authors declare no conflict of interest.

Data Availability Statement

The data that support the findings of this study are available from the corresponding author upon reasonable request.

Keywords

achilles tendon sleeve avulsion, anti-inflammatory, electroactive suture, PEDOT/HEC, tendon-bone regeneration

Received: June 23, 2025
Revised: August 6, 2025
Published online:

---

[1] N. Pien, H. Krzyslak, S. Shastry Kallaje, J. Van Meerssche, D. Mantovani, C. De Schauwer, P. Dubruel, S. Van Vlierberghe, C. P. Pennisi, *Appl. Mater. Today* **2023**, *31*, 101737.
[2] Z. Liu, G. Hou, W. Zhang, J. Lin, J. Yin, H. Chen, G. Huang, A. Li, *Injury* **2024**, *55*, 111207.
[3] J. Huh, M. E. Easley, J. A. Nunley, *Foot Ankle Int.* **2016**, *37*, 596.
[4] J. Y. Choi, S. S. Lee, T. H. Song, J. S. Suh, *Arch. Orthop. Trauma. Surg.* **2023**, *143*, 6513.
[5] M. T. Chorsi, E. J. Curry, H. T. Chorsi, R. Das, J. Baroody, P. K. Purohit, H. Ilies, T. D. Nguyen, *Adv. Mater.* **2018**, *31*, 1802084.
[6] S. Chen, X. Tong, Y. Huo, S. Liu, Y. Yin, M. L. Tan, K. Cai, W. Ji, *Adv. Mater.* *36*, **2024**, 2406192.
[7] G. Pavlou, R. Roach, S. Salehi-Bird, *Foot Ankle Int.* **2009**, *30*, 65.
[8] K. Beitzel, A. D. Mazzocca, E. Obopilwe, J. W. Boyle, J. McWilliam, L. Rincon, Y. Dhar, R. A. Arciero, A. Amendola, *Am. J. Sports Med.* **2013**, *41*, 1642.

[9] D. Ma, J. Wang, M. Zheng, Y. Zhang, J. Huang, W. Li, Y. Ding, Y. Zhang, S. Zhu, L. Wang, X. Wu, S. Guan, *Bioact. Mater.* **2023**, *26*, 128.
[10] M. Tao, Z. Fang, Y. Zhu, Y. Ju, Z. Hou, M. Fu, Z. Lu, D. Cai, J. Yang, J. Guo, *Bioact. Mater.* **2024**, *41*, 108.
[11] Z. Ge, Y. Qiao, W. Zhu, Y. Xu, Q. Fang, D. Wang, Y. Tang, R. Zhao, X. Deng, W. Lin, G. Wang, Y. Xiang, X. Hu, *Nano Energy* **2023**, *115*, 108751.
[12] L.-L. Zhao, J.-J. Luo, J. Cui, X. Li, R.-N. Hu, X.-Y. Xie, Y.-J. Zhang, W. Ding, L.-J. Ning, J.-C. Luo, T.-W. Qin, *ACS Appl. Mater. Interfaces* **2024**, *16*, 15879.
[13] S. Luo, C. Zhang, W. Xiong, Y. Song, Q. Wang, H. Zhang, S. Guo, S. Yang, H. Liu, *J. Orthop. Transl.* **2024**, *47*, 191.
[14] M. N. Gueye, A. Carella, J. Faure-Vincent, R. Demadrille, J.-P. Simonato, *Prog. Mater. Sci.* **2020**, *108*, 100616.
[15] N. A. A. Shahrim, Z. Ahmad, A. Wong Azman, Y. Fachmi Buys, N. Sarifuddin, *Mater. Adv.* **2021**, *2*, 7118.
[16] N. Li, Q. Yu, Y. D. Sidi Duan, X. Shi, X. Li, T. Jiao, Z. Qin, *Adv. Funct. Mater.* **2024**, *34*, 2309500.
[17] Y. Jiang, X. Dong, L. Sun, T. Liu, F. Qin, C. Xie, P. Jiang, L. Hu, X. Lu, X. Zhou, W. Meng, N. Li, C. J. Brabec, Y. Zhou, *Nat. Energy* **2022**, *7*, 352.
[18] F. Wang, Y. Kong, F. Shen, Y. Wang, D. Wang, Q. Li, *Composites, Part B* **2022**, *228*, 109436.
[19] L. Wang, X. He, Y. Hao, M. Zheng, R. Wang, J. Yu, X. Qin, *Sci. China Mater.* **2022**, *66*, 707.
[20] G. Kaur, G. E. Collis, R. Adhikari, P. Gunatillake, *Materials* **2024**, *17*, 4602.
[21] C. Yu, Z. Yue, H. Zhang, M. Shi, M. Yao, Q. Yu, M. Liu, B. Guo, H. Zhang, L. Tian, H. Sun, F. Yao, J. Li, *Adv. Funct. Mater.* **2023**, *33*, 2211023.
[22] T. Yang, M. Yang, C. Xu, K. Yang, Y. Su, Y. Ye, L. Dou, Q. Yang, W. Ke, B. Wang, Z. Luo, *J. Mater. Chem. B* **2023**, *11*, 3226.
[23] E. Petersohn Junior, C. Pires, R. A. de Freitas, W. L. E. Magalhaes, *Fibers Polym.* **2025**, *26*, 1465.
[24] N. A. Efiana, G. Kali, A. Fürst, A. Dizdarević, A. Bernkop-Schnürch, *Eur. J. Pharm. Sci.* **2023**, *180*, 106313.
[25] Y. Ye, L. Yu, E. Lizundia, Y. Zhu, C. Chen, F. Jiang, *Chem. Rev.* **2023**, *123*, 9204.
[26] W. Li, Y. Li, Z. Song, Y.-X. Wang, W. Hu, *Chem. Soc. Rev.* **2024**, *53*, 10575.
[27] A. F. Wibowo, S. Nagappan, S. A. Nurmaulia Entifar, J. H. Kim, Y. S. Sembiring, J. W. Han, J. Oh, G. Xie, J. Lee, J. Kim, D. C. Lim, M.-W. Moon, M.-S. Kim, S. Kim, Y. H. Kim, *J. Mater. Chem. A* **2024**, *12*, 19403.
[28] S. Wu, T. Dong, Y. Li, M. Sun, Y. Qi, J. Liu, M. A. Kuss, S. Chen, B. Duan, *Appl. Mater. Today* **2022**, *27*, 101473.
[29] Y. Xie, F. Zhang, O. Akkus, M. W. King, *J. Biomed. Mater. Res. B Appl. Biomater.* **2022**, *110*, 2624.
[30] X. Xu, Y. Si, Y. Zhao, Q. Ke, J. Hu, *Adv. Fiber Mater.* **2022**, *5*, 764.
[31] H. Yuan, X. Li, M.-S. Lee, Z. Zhang, B. Li, H. Xuan, W.-J. Li, Y. Zhang, *Int. J. Biol. Macromol.* **2021**, *170*, 248.
[32] L. Guo, H. Chen, Y. Li, J. Zhou, J. Chen, *Carbohydr. Polym.* **2023**, *299*, 120188.
[33] R. Gao, F. Li, Y. Zhang, P. Kong, Y. Gao, J. Wang, X. Liu, S. Li, L. Jiang, J. Zhang, C. Zhang, Z. Feng, P. Huang, W. Wang, *Biomater. Sci.* **2023**, *11*, 6573.
[34] M. Arif, J. Zhang, R. Xu, C. Yu, M. Majid, C. F. Guimarães, G. Li, T. Yu, Q. Zhou, R. L. Reis, *Adv. Healthc. Mater.* **2025**, 2502497.
[35] K. K. Das, B. Basu, P. Maiti, A. K. Dubey, *Appl. Mater. Today* **2024**, *39*, 102332.
[36] M. A. Marsudi, R. T. Ariski, A. Wibowo, G. Cooper, A. Barlian, R. Rachmantyo, P. J. D. S. Bartolo, *Int. J. Mol. Sci.* **2021**, *22*, 11543.
[37] X. Yu, G. Wu, P. Cai, Y. Ding, J. Cui, J. Wu, Y. Shen, J. Song, Z. Yuan, M. El-Newehy, M. M. Abdulhameed, H. Chen, X. Mo, B. Sun, Y. Yu, *ACS Appl. Mater. Interfaces* **2024**, *16*, 52104.
[38] I. M. Rothi, M. Åkerback, V. Bister, *J. Medical Case Rep.* **2023**, *17*, 155.
[39] X. Yu, Y. Shen, J. Cui, Y. Ding, Y. Morsi, B. Sun, X. Mo, H. Gu, *Med-X* **2025**, *3*, 7.
[40] J. Kim, H.-J. Kang, B.-S. Kim, Y.-M. Kim, H.-N. Kim, J.-Y. Park, Y.-R. Choi, A. Bat-Ulzii, J. Cho, *J. Environ. Res, Public Health* **2022**, *19*, 12897.
[41] X. Yu, G. Wu, Y. Ding, P. Shang, P. Cai, J. Cui, J. Song, J. Wu, M. El-Newehy, M. M. Abdulhameed, X. Mo, Y. Yu, B. Sun, *Acta Biomater.* **2025**, *197*, 202.
[42] M. Pluchino, L. Vivarelli, G. Giavaresi, D. Dallari, M. Govoni, *J. Funct. Biomater.* **2025**, *16*, 130.
[43] B. S. Heidari, R. Ruan, E. Vahabli, P. Chen, E. M. De-Juan-Pardo, M. Zheng, B. Doyle, *Bioact. Mater.* **2023**, *19*, 179.
[44] A. Escobar, A. Serafin, M. R. Carvalho, M. Culebras, A. Cantarero, A. Beaucamp, R. L. Reis, J. M. Oliveira, M. N. Collins, *Adv. Compos. Hybrid Mater.* **2023**, *6*, 118.
[45] M. E. Martinez-Cartagena, N. Muzzio, G. Romero, J. Bernal-Martinez, D. Martinez-Lara, J. Moncivaiz-Medina, M. Román-Aguirre, A. Aguilar-Eguezabal, N. Cuando-Espitia, *Mater. Today Chem.* **2023**, *34*, 101817.
[46] X. Jia, X. Ma, L. Zhao, M. Xin, Y. Hao, P. Sun, C. Wang, D. Chao, F. Liu, C. Wang, G. Lu, G. Wallace, *Chem. Sci.* **2023**, *14*, 2123.
[47] G. A. Hjorthaug, J. E. Madsen, L. Nordsletten, F. P. Reinholt, H. Steen, S. Dimmen, *J. Orthop. Res.* **2014**, *33*, 216.
[48] S. Jiang, X. Zhao, S. Chen, G. Pan, J. Song, N. He, F. Li, W. Cui, C. Fan, *Biomaterials* **2014**, *35*, 9920.
[49] X. Liu, X. He, D. Jin, S. Wu, H. Wang, M. Yin, A. Aldalbahi, M. El-Newehy, X. Mo, J. Wu, *Acta Biomater.* **2020**, *108*, 207.